Mesospheric Q2DW interactions with four migrating tides at 53°N latitude: zonal wavenumber identification through dual-station approaches

Maosheng He[1], Jeffrey M Forbes[2], Guozhu Li[3], Christoph Jacobi[4], and Peter Hoffmann[1]

[1]Leibniz-Institute of Atmospheric Physics at the Rostock University
[2]University of Colorado Boulder
[3]Institute of Geology and Geophysics, Chinese Academy of Sciences
[4]Institut fur Meteorologie, Universitat Leipzig, Germany

November 26, 2022

Abstract

Mesospheric winds from two longitudinal sectors at 53°N latitude are combined to investigate quasi-two-days (Q2DWs) and their nonlinear interactions with tides. In a summer 2019 case study, we diagnose the zonal wavenumber m of spectral peaks at expected frequencies through two dual-station approaches, a phase differencing technique (PDT) on individual spectral peaks and a least-squares procedure on family-batched peaks. Consistent results from the approaches verify the occurrences of Rossby-gravity modes (m=3 and 4 at periods T= 2.1d and 1.7d), and their secondary waves (SWs) generated from interactions with diurnal, semi-diurnal, ter-diurnal and quatra-diurnal migrating tides. We further extend the PDT to 2012–2019, illustrating that Q2DWs exhibit significant interannual variability. Composite analysis reveals seasonal and altitude variations of the Rossby-gravity modes and their SWs. The Rossby-gravity modes maximize in local summer, whereas their 16- and 9.6-hr SWs appear more in winter, potentially originating from Q2DW-tide interactions in the opposite hemisphere.

Mesospheric Q2DW interactions with four migrating tides at 53°N latitude: zonal wavenumber identification through dual-station approaches

Maosheng He[1], Jeffrey M. Forbes[2], Guozhu Li [3,4], Christoph Jacobi[5], Peter Hoffmann[1]

[1]Leibniz-Institute of Atmospheric Physics at the Rostock University, Kühlungsborn, Germany
[2]Ann & H.J. Smead Department of Aerospace Engineering Sciences, University of Colorado, Boulder, USA
[3]Beijing national observatory of space environment, Institute of Geology and Geophysics, Chinese Academy of Sciences, Beijing, China
[4]College of Earth and Planetary Sciences, University of Chinese Academy of Sciences, Beijing, China
[5]Institute for Meteorology, Universität Leipzig, Leipzig, Germany

Key Points:

- Multi-station approaches are developed to diagnose zonal wavenumber m of near-2d, -16hr, -9.6hr and -6.9hr spectral peaks
- Diagnosed are Rossby-gravity modes with m=3, and 4 and their SWs from non-linear interactions with 24hr, 12hr, 8hr and 6hr migrating tides.
- The Rossby-gravity modes maximize in the local summer, whereas their SWs maximize in the local winter.

Index Terms: 3389, 3332, 6994, 3334, 4455

Key words: quasi-two-days, atmosphere-ionosphere coupling Rossby-gravity wave, mesosphere, cross-wavelet, zonal wavenumber

---

Corresponding author: He, M., `he@iap-kborn.de`

Abstract

Mesospheric winds from two longitudinal sectors at 53°N latitude are combined to investigate quasi-two-days (Q2DWs) and their nonlinear interactions with tides. In a summer 2019 case study, we diagnose the zonal wavenumber m of spectral peaks at expected frequencies through two dual-station approaches, a phase differencing technique (PDT) on individual spectral peaks and a least-squares procedure on family-batched peaks. Consistent results from the approaches verify the occurrences of Rossby-gravity modes (m=3 and 4 at periods T= 2.1d and 1.7d), and their secondary waves (SWs) generated from interactions with diurnal, semi-diurnal, ter-diurnal and quatra-diurnal migrating tides. We further extend the PDT to 2012–2019, illustrating that Q2DWs exhibit significant interannual variability. Composite analysis reveals seasonal and altitude variations of the Rossby-gravity modes and their SWs. The Rossby-gravity modes maximize in local summer, whereas their 16- and 9.6-hr SWs appear more in winter, potentially originating from Q2DW-tide interactions in the opposite hemisphere.

Plain Language Summary

The quasi-two-day wave is the strongest and most widely-studied planetary wave occurring in the mesosphere. Existing observational analyses are based on either single-satellite or -station approaches, which suffer from temporal and spatial aliasing, respectively. The current study implements and develops dual-station approaches to investigate the mesospheric quasi-two-day wave at 53°N latitude, in a case and a statistical study. Our approaches allow diagnosing both the frequency and zonal wavenumber. In the case study, we diagnosed two Rossby-gravity modes and the secondary waves of the nonlinear interactions between the Rossby-gravity modes and the migrating tides at periods of 24, 12, 8, and 6hr. While the interactions with the 24 and 12hr tides are expected, those with the 8 and 6hr tides are reported for the first time. In the statistical study, we report the seasonality and altitude variation of the Rossby-gravity modes and their most dominant secondary waves.

1 Introduction

The quasi-two-day wave (Q2DW) is perhaps the largest and most widely-studied planetary wave (PW) in the mesosphere. An excellent historical account of observational, theoretical and modeling studies of the Q2DW is given by Tunbridge et al. (2011). Briefly, the Q2DW was first discovered in meteor radar winds (Muller, 1972; Babadshanov et al., 1973), and was later proposed theoretically to be the atmospheric manifestation of the gravest westward-propagating Rossby-gravity normal mode with zonal wavenumber $m = 3$ (Salby & Roper, 1980; Salby, 1981; Salby & Callaghan, 2001). An alternative explanation (Plumb, 1983; Pfister, 1985) was that the Q2DW is the response to instability in the mesospheric summer westward jet, with potential zonal wavenumbers m=2–4. It seems likely that the Q2DW is a near-resonant oscillation excited and/or amplified by an instability (Randel, 1994). Within the satellite era, various space-based observations have been explored to study the Q2DW (e.g., Huang et al., 2013; Moudden & Forbes, 2014; Pancheva et al., 2018), delineating seasonal-latitudinal and interannual variabilities of Q2DWs with m= 2, 3, and 4 (as summarized by Tunbridge et al., 2011). Insightful analyses on the Q2DW have also been performed in the context of a global middle atmosphere data assimilation model (Pancheva et al., 2016; Lieberman et al., 2017).

An intriguing aspect of the early radar studies was the discovery (e.g., Manson et al., 1982) that nonlinear interaction between the Q2DW and the semi-diurnal tide yields 9.6hr and 16hr secondary waves (SWs) which are sometimes observed in the wind spectra (e.g., Cevolani & Kingsley, 1992; Beard et al., 1999). The underlying theory was further developed (Teitelbaum et al., 1989; Teitelbaum & Vial, 1991) to include longitude dependence of the waves, tide-tide and other PW-tide interactions. The interactions are regulated by the resonance conditions (e.g., Teitelbaum & Vial, 1991; He et al., 2017). Assume that at longitude λ and time t, the disturbance, induced by a zonal traveling wave with an amplitude $\tilde{\alpha}$ and zonal wavenumber m at frequency f, could be represented as,

$$\tilde{\Psi}(\tilde{\alpha}, f, m|\lambda, t) := \tilde{\alpha}\tilde{\psi}(f, m|\lambda, t) := \tilde{\alpha}e^{2\pi i(ft+m\lambda)} \tag{1}$$

Then, two waves, $\tilde{\alpha}_1\tilde{\psi}_1(f_1, m_1|\lambda, t)$ and $\tilde{\alpha}_2\tilde{\psi}_2(f_2, m_2|\lambda, t)$, might interact nonlinearly and generate a SW, $\tilde{\alpha}_{SW}\tilde{\psi}_{SW}(f_{SW}, m_{SW}|\lambda, t)$. The resonance conditions specify,

$$\tilde{\psi}_{SW} = \tilde{\psi}_1\tilde{\psi}_2, \tilde{\psi}_1\tilde{\psi}_2^*, \tilde{\psi}_1^*\tilde{\psi}_2, \text{or}, \tilde{\psi}_1^*\tilde{\psi}_2^* \quad (2)$$

Hereafter, $\tilde{\bullet}^*$, $\Re(\tilde{\bullet})$, and $\arg\{\tilde{\bullet}\}$ denote the conjugate, real part, and argument (in the range from 0 to 2π excluding 2π) of a complex value $\tilde{\bullet}$, respectively. Since $\Re(\tilde{\psi}_1\tilde{\psi}_2^*)=$ $\Re(\tilde{\psi}_1^*\tilde{\psi}_2)$, $\tilde{\psi}_1\tilde{\psi}_2^*$ and $\tilde{\psi}_1^*\tilde{\psi}_2$ represent the same wave, and so do $\tilde{\psi}_1^*\tilde{\psi}_2^*$ and $\tilde{\psi}_1\tilde{\psi}_2$. Therefore, there are two independent SWs, $\Re(\tilde{\psi}_1\tilde{\psi}_2)$ and $\Re(\tilde{\psi}_1\tilde{\psi}_2^*)$, termed hereafter as upper and lower sidebands (USB and LSB), respectively.

Equation 2 implies,

$$f_{SW} = f_1 \pm f_2, \text{and}, m_{SW} = m_1 \pm m_2 \quad (3)$$

According to Equation 3, the interactions between the Rossby-gravity (R-G) modes (Q2DWs with m=3 and 4, Q2DW3 and Q2DW4) and the diurnal and semi-diurnal migrating tides (DW1 and SW2, at f=1 and 2cpd with m=1 and 2, respectively) could generate up to eight SWs. The SWs populate at three periods, 2d, 16hr, and 9.6hr with different m, as displayed in the f-m depiction in Figure 1a. In addition, these three periods are also populated by SWs of interactions between Q2DWs and various non-migrating tides (Forbes & Moudden, 2012).

The importance of SWs arising from Q2DW-tide interactions to atmosphere-ionosphere (A-I) coupling was recently demonstrated using a whole-atmosphere-ionosphere general circulation model (e.g., Gu et al., 2018). Although the Q2DW may or may not penetrate above the mesopause (Salby & Callaghan, 2001), depending on background wind conditions, a subset of the SWs can propagate well into the E-region (Palo et al., 1999; Nguyen et al., 2016; Gu et al., 2018) and generate electric fields that carry the Q2DW periodicity to the F-region (Gu et al., 2018). The point here is that eastward- (westward-) propagating waves favor propagation into regions of prevailing westward (eastward) zonal-mean zonal winds. The presence of SWs in the wind spectrum is significant since they propagate freely as independent oscillations and contribute measurably to the longitude-time structure and complexity of the overall dynamics (Gu et al., 2018; Pedatella & Forbes, 2012), and to the ionospheric response (e.g., Gu et al., 2018). A major challenge to date has been our inability to unequivocally determine which 9.6h and 16h waves are present in the atmosphere at any given time. As noted above, while SWs at expected frequencies have been observed using ground-based observations, these observations provide no information on m of the SWs, and therefore their capability to propagate to higher altitudes. From the vantage point of single-satellite missions in quasi-sun-synchronous orbits, any Q2DW (at f=0.5cpd with any m) and all its SWs from interactions with all migrating tides will be Doppler-shifted to the same frequency $f' = |m–0.5|$ cpd, and therefore cannot be distinguished from each other. The quantity $|m–0.5|$ is also discussed as the apparent or spaced-based zonal wavenumber. Forbes and Moudden (2012) specified the apparent wavenumbers of the Q2DW SWs associated with various migrating and non-migrating tides (described also from a somewhat different perspective in Nguyen et al., 2016).

In summary, single-satellite or -station approaches suffer from temporal and spatial aliasing (cf, Appendix A in He, Chau, et al., 2020), respectively. In the present paper, we use two dual-station approaches, one developed in the current work and the other called the phase differencing technique (PDT) developed in He, Chau, Stober, et al. (2018), to identify f and ms of diverse SWs arising from Q2DW-tide interactions. Consistent results from the approaches reveal that Q2DW-tide interactions are more diverse than the expectation according to the existing knowledge.

2 Data analysis

According to Equation 1, we define $\tilde{a}(\lambda) := \tilde{\alpha}e^{2\pi im\lambda}$. Assume that $\tilde{a}(\lambda_1)$ and $\tilde{a}(\lambda_2)$ are the observational estimations of $\tilde{a}(\lambda)$ at two longitudes λ_1 and λ_2. Then, their cross product is,

$$\tilde{c} := \tilde{a}(\lambda_1)\tilde{a}^*(\lambda_2) = |\tilde{\alpha}|^2 e^{im(\lambda_1-\lambda_2)} := |\tilde{\alpha}|^2 e^{im\lambda_\Delta} \tag{4}$$

Equation 4 presents the possibility to estimate m,

$$m = \frac{\arg\{\tilde{c}\} + 2Z\pi}{\lambda_\Delta} = \frac{\arg\{\tilde{c}\}}{\lambda_\Delta} + \frac{2\pi Z}{\lambda_\Delta} := m_0 + Z\Delta_m \tag{5}$$

Here, $\arg\{\tilde{c}\}+2\pi Z$ represents the phase difference between the longitudes, where $Z \in \mathbb{Z}$ is an integer representing a whole-cycle ambiguity. All possible m values are aliases of m_0, and Δ_m denotes the Nyquist sampling theorem in the spatial domain. Below, we implement the PDT on mesospheric zonal and meridional winds u and v over two sites, Mohe (M, 122°E, 54°N) and the northern part of Germany (G, 13°E, 53°N). The wind over Mohe is detected by a meteor radar (Yu et al., 2013), whereas the wind over Germany is derived with echoes from two individual radars at Juliusruh (13°E, 55°N, Hoffmann et al., 2010) and Collm (13°E, 51°N, Jacobi, 2012; Lilienthal & Jacobi, 2015) to expand the data coverage at this longitude. Hourly winds are estimated on an altitude grid h=80.5,81.5,... 99.5km through the approach presented in Hocking et al. (2001).

Below we present a case and statistical studies in Sections 3 and 4, respectively.

3 A case study

The zonal wind u and meridional wind v between 1 June and 15 September 2019 are used to calculate the Lomb-Scargle spectra, yielding complex amplitudes for the Mohe and German radar systems $\tilde{a}_u^M$, $\tilde{a}_v^M$, $\tilde{a}_u^G$, and $\tilde{a}_v^G$, at each individual altitude. The amplitudes are used to calculate $\langle|\tilde{a}_u^2|+|\tilde{a}_v^2|\rangle$ averaged between G and M, for which the amplitudes below the significance level $\alpha = 0.05$ are set to zero. The average is displayed in Figure 2a. At h >96km in Figure 2a the spectrum is noisy, potentially due to the relatively low density of the meteor distribution and high plasma density. Therefore, the current work focuses mainly on the altitude below 96km. To implement Equation 4, we calculate the cross product $\tilde{c}_u := \tilde{a}_u^{M*}\tilde{a}_u^G$ and $\tilde{c}_v := \tilde{a}_v^{M*}\tilde{a}_v^G$, and calculate the altitude average $\tilde{c} := \langle\tilde{c}_u + \tilde{c}_v\rangle_{80<h<96\mathrm{km}}$ displayed in Figure 2b. To inspect the details in Figure 2b, we develop a representation for the spectrum in Section 3.1, with which we estimate m of spectral peaks using two approaches. The results are summarized in Figure 1b and Table 1 and explained below.

3.1 Spectral periodic table

We divide the $\tilde{c}(f)$ spectrum in Figure 2b into 0.5cpd-wide pieces, as denoted by the color bars on the top of Figure 2b, indexed as '$N\pm$', i.e., '0+','1−','1+',...,'3+'. Each of the pieces is zoomed into one row in Figure 2c. Note that in Figure 2c the x-axis represents $|\delta f| := |f-\lfloor f \rceil|$, namely, the distance between f and its nearest integer $\lfloor f \rceil$. We call the representation of Figure 2c as the spectral periodic table. According to Equation 3, SWs of all potential interactions between a wave at given frequency f_2 >0 and all tides at f_1=1cpd, 2cpd,... will share the same $|\delta f|$= $|f_2-\lfloor f_2 \rceil|$ and therefore are located at the same column in the spectral periodic table.

3.2 The tidal signatures

At the top of Figure 2c, there are short horizontal bars in black, blue and red, corresponding to the three maximum peaks of $P(|\delta f|) := \prod_{N\pm} |\tilde{c}(|\delta f|)|$. Each of these bars represents a 0.015cpd-wide δf interval, narrower than the spectral frequency resolution $2\sigma_f \sim 2/T_w = 2/106\text{d} = 0.019\text{cpd}$. Here, T_w=106d is the window width. For example, the black bar corresponds to δf=0±0.0075cpd.

At δf=0±0.0075cpd in each row of Figure 2c, we search for a maximum spectral peak, displayed as the vertical black lines in Figures 2b–c and specified in black in Table 1. The $\tilde{c}$ values of these maximum peaks are input into Equation 5 to estimate m, resulting in m^{PDT} listed in black in Table 1. According to Equation 5, all solutions m^{PDT} comprise aliases denoted by $Z\Delta_m$, where Δ_m=3.31 is determined by our radar separation. At f =1.0cpd and when Z=0, the PDT estimation is m^{PDT}=0.95+3.31Z=0.95 when Z=0. At f =2.0, 3.0, and 4.0cpd, m^{PDT}=1.09, 3.46, and 3.56 when Z=0,1, and 1, respectively. The nearest integers of m^{PDT} are $\lfloor m^{PDT} \rceil$=1, 2, 3, and 4, as listed in the column 'm^f' in Table 1. Therefore, we explain the corresponding spectral peaks as migrating solar tides, DW1 SW2, TW3, and QW4 (diurnal, and semi-, ter-, and quatra-diurnal westward traveling tides with m=1, 2, 3, and 4).

3.3 The Q2DW4 family

Similarly, at $|\delta f|$=0.4275±0.0075cpd, denoted by the blue bar on the top of Figure 2c, we search for the maximum peak in each row of Figure 2c, above a threshold value $\sqrt{|\tilde{c}|}$ >1.1m/s that is the QW4 tidal amplitude from the previous subsection. Six maxima are searched, displayed as the vertical blue lines in Figures 2b–c, whose frequencies and $\tilde{c}$ values (denoted as $\tilde{c}_{N\pm}$) are specified in blue in Table 1. $\tilde{c}_{N\pm}$ are used to estimate the corresponding wavenumber $m_{N\pm}$ through PDT according to Equation 5, resulting in $m^{PDT}_{N\pm}$ specified in Table 1. To deal with the ambiguities represented by Z in $m^{PDT}_{N\pm}$, below we present a family-batched estimation of $m_{N\pm}$. According to Equation 4,

$$\tilde{c}_{N\pm}/|\tilde{c}_{N\pm}| = e^{im_{N\pm}\lambda_\Delta} \tag{6}$$

Here, $m_{N\pm}$ might not be completely independent but generate each other by interacting nonlinearly with the tides identified in Section 3.2, and therefore are regulated by the resonance conditions in Equation 3. In the most extreme case, only one wave is independent and all the others are associated SWs. In this single-independent-wave case, only one wavenumber is independent and $m_{N\pm}$ can be represented as:

$$m_{N\pm} = N \pm m_{0+} \tag{7}$$

Substituting Equation 7 into Equation 6, yielding,

$$\tilde{c}_{N\pm}/|\tilde{c}_{N\pm}| = e^{i(N \pm m_{0+})\lambda_\Delta} \Rightarrow e^{-iN\lambda_\Delta}\tilde{c}_{N\pm}/|\tilde{c}_{N\pm}| = e^{\pm i m_{0+}\lambda_\Delta} \tag{8}$$

which is an overdetermined system comprised of only one unknown m_{0+} and six equations. We first estimate the least-squares solution of $e^{im_{0+}}$ denoted as $\tilde{e}_{LS}$, and then estimate m_{0+} through an optimization $m^f_{0+} = \underset{\hat{m}}{\operatorname{argmax}} \Re(\tilde{e}^*_{LS} e^{i\hat{m}})$, subject to: $\hat{m} \in [-5, -3, ..., 5]$. Here, we use the superscript f to distinguish the family-batched estimations $m^f_{N\pm}$ from the PDT estimations $m^{PDT}_{N\pm}$.

Solving the optimization yields the estimation $m^f_{0+} = -3$. Other $m^f_{N\pm}$ are calculated according to Equation 7, listed in blue in the column 'm^f' in Table 1. At each of the six estimations, $m^f_{N\pm}$ is compared with $m^{PDT}_{N\pm}$. The comparison results are listed in the column '$m^f \approx m^{PDT}$' in Table 1, in which checkmarks '✓' denote consistencies between $m^f_{N\pm}$ and $m^{PDT}_{N\pm}$ whereas the cross mark '×' denotes an inconsistency. The consistency is claimed if $\exists Z$: $\lfloor m^{PDT}_{N\pm}(Z) \rceil = m^f_{N\pm}$ which equals to,

$$\delta m_{N\pm} := \min |m^{PDT}_{N\pm} - m^f_{N\pm}| < 0.5 \tag{9}$$

Among the six estimations, five estimations exhibit consistency, among which the one at f=0.58cpd could be explained as the R-G mode Q2DW4 (e.g., Salby & Callaghan, 2001). Accordingly, we explain the remaining four as the SWs of tide±Q2DW4 interactions as specified in the last column in Table 1. (Here, '+' and '–' represent the USB- and LSB-generating interactions, respectively.) The blue symbols in Figure 1b present the five consistent estimations in the f-m plane.

3.4 The Q2DW3 family

Further, we implement the above peak identification, least-squares estimation, and optimization, at $|\delta f|$= 0.4775±0.0075cpd denoted by the red bar on the top of Figure 2c. The results are displayed as the vertical red lines in Figures 2b–c and specified in red in Table 1. The family-batched estimation m^f and the individual PDT estimation m^{PDT} are consistent for all six peaks, denoted as the red symbols in Figure 1b. Among the six peaks, the one at f=0.485cpd is explained as the Q2DW R-G mode with m^f=3 (Q2DW3, e.g., Salby & Roper, 1980). Therefore, the remaining five peaks are explained in terms of migrating tides±Q2DW3 interactions as specified in the last column in Table 1.

To our knowledge, the interactions of the R-G modes with TW3 and QW4 are reported here for the first time.

4 2012–2019 composite analysis

The previous section implements the PDT in a case study through Lomb-Scargle spectral analysis. In the current section, we replace the Lomb-Scargle spectral analysis with cross wavelet (CWL) analysis (following, e.g., He, Yamazaki, et al., 2020; He, Chau, Hall, et al., 2018), to implement PDT to a statistical analysis using the data between January 2012 and December 2019. We first calculate the Gabor wavelet (Torrence & Compo, 1998) of the u and v components over Germany and Mohe at each altitude h, resulting in amplitudes $\tilde{W}^{G,u,h}_{(f,t)}$, $\tilde{W}^{G,v,h}_{(f,t)}$,$\tilde{W}^{M,u,h}_{(f,t)}$, and $\tilde{W}^{M,v,h}_{(f,t)}$. These amplitudes are the observational estimations of $\tilde{a}(\lambda)$ in Equation 4, and are functions of t and f. Then, the cross product $\tilde{C} := \tilde{W}^{G*}_{(f,t)}\tilde{W}^{M}_{(f,t)}$, namely, the CWL spectrum, is the observational estimation of $\tilde{c}$ in Equation 4. We sum the CWL spectra of the u and v components, yielding $\tilde{C}_{u+v} :=\tilde{C}_u+\tilde{C}_v$. Below, in Sections 4.1 and 4.2 we inspect the f-t depiction of altitude-averaged $\tilde{C}_{u+v}$ and h-t depiction of $\tilde{C}_{u+v}$ at discrete frequencies, respectively.

4.1 Altitude-averaged CWL spectrum

Figure 3a displays $\langle\tilde{C}_{u+v}\rangle_{80<h<96\text{km}}$, in which the darkness represents the magnitude while the color hue denotes its phase. The magnitude exhibits an annual variation, maximizing in local summer (July–September) with dim spectral peaks in local winter.

The $\langle\tilde{C}_{u+v}\rangle_h$ in Figure 3a is composited as a function of the month, displayed in Figure 3b. As indicated by the black dashed line in Figure 3b, the composited spectrum maximizes largely earlier at a higher frequency. Below, we mainly focus on the frequency range Δf_{Q2DW}:=[0.40 0.60cpd] where the strongest spectral peaks occur. The strongest two peaks are the red one at f=0.57–0.60cpd (T=40.0–42.1hr) and the blue at f=0.48–0.50cpd (T=48.0–50.0hr), both of which appear in July. The redness and blueness are associated with m=4 and 3, respectively. These two peaks can be explained as R-G modes Q2DW4 and Q2DW3, because both their f and m are consistent with the theoretical expectations [T,m] =[1.7d, 4] and [2.1d, 3] (cf, Salby & Callaghan, 2001). Except for the red and blue peaks, Figure 3b is dominated mainly by magenta associated with m=–3 (Q2DE3), including a peak at f=0.52–0.55cpd in July and the smeared region within f=0.35–0.50cpd in August. The smeared Q2DE3 signature could be explained as the LSB of the interaction between DW1 and Q2DW4 at f=0.57–0.60cpd, whereas the Q2DE3 peak at f=0.52–0.55cpd might not be excited in-situ as no Q2DW4 signature appears at the required frequency.

The above four Q2DW signatures exhibit significant interannual variabilities, as revealed in Figure 3a. The Q2DW3 signature occurred in summers of 2012, 2013, 2016, and 2019; the Q2DW4 occurred in 2012, 2013, 2017, and 2019; the Q2DE3 signature at f=0.35–0.50cpd occurred weakly in 2012, 2014, 2015, 2016, and 2017; and the Q2DE3 signature at f=0.50–0.55cpd occurred in 2012, 2014, 2015, 2016, and 2017. Besides, also between f=0.45cpd and 0.55cpd occurred the green peak in 2012, 2014, 2018 and 2019, which is not visible in the composited spectrum. The greenness suggests m=2, (e.g., Tunbridge et al., 2011).

Figures 3c–d present the same plots as Figure 3b but for periods near 16hr and 9hr, namely, frequency ranges of the SWs. Given that in Figures 3b Q2DWs occur mainly within the Δf_{Q2DW}=[0.40 0.60cpd], we focus hereafter on Δf_{Q2DW}+1cpd and Δf_{Q2DW}+2cpd. In these ranges, the spectra maximize annually during December–January, when the southern hemispheric Q2DW maximizes (e.g., Salby & Callaghan, 2001). The SWs associated with the southern hemispheric Q2DWs-tides interactions might extend to northern hemispheric mid-latitudes. In Figure 3, SWs are weaker in the summer than that in the winter, possibly due to the preference of the southern hemispheric Q2DW towards periods between 48–52hr and m=3 (e.g., Tunbridge et al., 2011), whereas the northern hemispheric Q2DW tends to spread out in period and zonal wavenumber. This suggests that the southern hemispheric SWs would be more repeatable from year to year.

4.2 Altitude variation

Figure 4 displays the composited spectra of $\tilde{C}_{u+v}$ as a function of the month and altitude at the frequencies illustrated by the horizontal gray dashed lines in Figures 3b–d. Figures 4a and 4b capture the Q2DW3 and Q2DW4, respectively. While the Q2DW3 occurs mainly above 90km, the Q2DW4 peak extends to a lower altitude. Such a difference could be observed in the geopotential amplitudes at southern hemispheric mid-latitude in a theoretical computation (Figures 6 vs. 10 in Salby & Callaghan, 2001). The computation suggests that the Q2DW4 is strongly distorted by the mean wind and does not penetrate much across the mesopause whereas the Q2DW3 extends upward into the thermosphere.

In Figure 1, there are four near-16hr SWs (m= –2, –1, 4, and 5), and four near-9hr SWs (m=–1, 0, 5, and 6). Among the potential near-16hr SWs, the m=4 in Figure 4c is the strongest one. In the case of near-9hr SWs, the m=0 appears in Figure 4f while m=–1 and 6 occur in Figure 4e. Both the near-16hr and -9hr SWs maximize in the local winter. In August–September in Figures 4c–d, near-16hr SWs occur only at high altitudes. .

5 Summary

Mesospheric winds, from two longitudinal sectors at 53°N, are combined to investigate the Q2DW in a summer 2019 case study and an 8-year statistical study. In the case study, PDT is first implemented to diagnose zonal wavenumber m of the Lomb-Scargle cross-spectral peaks at T =24, 12, 8, and 6hr, suggesting migrating tides, DW1, SW2, TW3, and QW4. Then, we arrange the cross-spectrum into a periodic table to batch spectral peaks of each expected Q2DW and all its potential SWs into one family. For each family, we estimate m through two approaches, the PDT on individual peaks and a family-batched estimation. Consistent estimations of the approaches suggest two families, namely Q2DW3 with its five SWs, and Q2DW4 with its four SWs. These SWs entail tidal waves of DW1, SW2, TW3, and QW4, among which TW3 and QW4 are reported for the first time as the parent waves.

In the statistical study, cross-wavelet analysis is implemented to the wind observations between 2012 and 2019. The cross-wavelet spectra are composited into frequency-month (f-t) depictions in three period ranges near-2d, -16hr and -9.6hr and altitude-month (h-t) depictions at discrete frequencies. The near-2d spectrum exhibits significant inter-annual variabilities and seasonal variation, which maximizes in July at f=0.57–0.60cpd, 0.48–0.50cpd, and 0.50–0.55cpd (T=40.0–42.1hr, 48.0–50.0hr, and 48.0–43.6hr) associated with m=3, 4, and –3, first two of which are R-G modes. The near-16hr and -9.6hr spectra maximize in local winter when the near-2d spectra are weak locally and maximize in the southern hemisphere, suggesting that SWs of Q2DW-tide interactions in the southern hemisphere extend into northern hemispheric mid-latitudes. The Q2DWs and their SWs exhibit various altitude distributions: (1) in summer, the Q2DW4 peak extends to low altitudes than Q2DW3, and (2) the summer near-16hr SWs are distributed at a higher altitude than those in the winter. Given the potential relevance to global atmosphere-ionosphere coupling, the mechanisms underlying the height and seasonal-latitudinal behaviors of SWs revealed here warrant study by global models.

Acknowledgments

MH, JMF and GL are supported by the Deutsche Forschungsgemeinschaft through grant CH1482/1-2, NSF Award AGS-1630177 to the University of Colorado Boulder, the National Natural Science Foundation of China (42020104002), respectively. The Mohe data is provided by the WDC for Geophysics (http://wdc.geophys.ac.cn/), at BNOSE, IGGCAS. The post-processed data used in the current paper are available at the Harvard Dataverse through https://doi.org/10.7910/DVN/GCLHLV.

References

Babadshanov, P. B., Kalchenko, B. V., Kashcheyev, B. L., & Fedynsky, V. V. (1973). Winds in the equatorial lower thermosphere. *Proc. Acad. Sci. USSR*, *208*, 1334–1337.

Beard, A. G., Mitchell, N. J. J., Williams, P. J. S. J. S., & Kunitake, M. (1999). Non-linear interactions between tides and planetary waves resulting in periodic tidal variability. *J. Atmos. Solar-Terrestrial Phys.*, *61*(5), 363–376. doi: 10.1016/S1364-6826(99)00003-6

Cevolani, G., & Kingsley, S. P. (1992). Non-linear effects on tidal and planetary waves in the lower thermosphere: Preliminary results. *Adv. Sp. Res.*, *12*(10), 77–80. doi: 10.1016/0273-1177(92)90446-5

Forbes, J. M., & Moudden, Y. (2012). Quasi-two-day wave-tide interactions as revealed in satellite observations. *J. Geophys. Res. Atmos.*, *117*(12). Retrieved from `https://agupubs.onlinelibrary.wiley.com/doi/abs/10.1029/2011JD017114` doi: 10.1029/2011JD017114

Gu, S. Y., Liu, H. L., Dou, X., & Jia, M. (2018). Ionospheric Variability Due to Tides and Quasi-Two Day Wave Interactions. *J. Geophys. Res. Sp. Phys.*, *123*(2), 1554–1565. doi: 10.1002/2017JA025105

He, M., Chau, J. L., Forbes, J. M., Thorsen, D., Li, G., Siddiqui, T. A., . . . Hocking, W. K. (2020). Quasi-10-day wave and semi-diurnal tide nonlinear interactions during the southern hemispheric SSW 2019 observed in the northern hemispheric mesosphere. *Earth Sp. Sci. Open Arch.*, 22. Retrieved from `https://doi.org/10.1002/essoar.10503943.1` doi: 10.1002/essoar.10503943.1

He, M., Chau, J. L., Hall, C. M., Tsutsumi, M., Meek, C., & Hoffmann, P. (2018). The 16-Day Planetary Wave Triggers the SW1-Tidal-Like Signatures During 2009 Sudden Stratospheric Warming. *Geophys. Res. Lett.*, *45*(22), 12,631–12,638. Retrieved from `http://doi.wiley.com/10.1029/2018GL079798` doi: 10.1029/2018GL079798

He, M., Chau, J. L., Stober, G., Hall, C. M., Tsutsumi, M., & Hoffmann, P. (2017). Application of Manley-Rowe Relation in Analyzing Nonlinear Interactions Between Planetary Waves and the Solar Semidiurnal Tide During 2009 Sudden Stratospheric Warming Event. *J. Geophys. Res. Sp. Phys.*, *122*(10), 10,783–10,795. Retrieved from `http://dx.doi.org/10.1002/2017JA024630` doi: 10.1002/2017JA024630

He, M., Chau, J. L., Stober, G., Li, G., Ning, B., & Hoffmann, P. (2018). Relations Between Semidiurnal Tidal Variants Through Diagnosing the Zonal Wavenumber Using a Phase Differencing Technique Based on Two Ground-Based Detectors. *J. Geophys. Res. Atmos.*, *123*(8), 4015–4026. Retrieved from `http://doi.wiley.com/10.1002/2018JD028400` doi: 10.1002/2018JD028400

He, M., Yamazaki, Y., Hoffmann, P., Hall, C. M., Tsutsumi, M., Li, G., & Chau, J. L. (2020). Zonal Wave Number Diagnosis of Rossby Wave-Like Oscillations Using Paired Ground-Based Radars. *J. Geophys. Res. Atmos.*, *125*(12). Retrieved from `https://doi.org/10.1029/2019JD031599` doi: 10.1029/2019JD031599

Hocking, W. K., Fuller, B., & Vandepeer, B. (2001). Real-time determination of meteor-related parameters utilizing modern digital technology. *J. Atmos. Solar-Terrestrial Phys.*, *63*(2), 155–169. Retrieved from `http://www.sciencedirect.com/science/article/pii/S1364682600001383` doi:

https://doi.org/10.1016/S1364-6826(00)00138-3

Hoffmann, P., Becker, E., Singer, W., & Placke, M. (2010). Seasonal variation of mesospheric waves at northern middle and high latitudes. *J. Atmos. Solar-Terrestrial Phys.*, *72*(14), 1068–1079. Retrieved from http://www.sciencedirect.com/science/article/pii/S1364682610001987 doi: https://doi.org/10.1016/j.jastp.2010.07.002

Huang, Y. Y., Zhang, S. D., Yi, F., Huang, C. M., Huang, K. M., Gan, Q., & Gong, Y. (2013). Global climatological variability of quasi-two-day waves revealed by TIMED/SABER observations. *Ann. Geophys.*, *31*(6), 1061–1075. Retrieved from https://angeo.copernicus.org/articles/31/1061/2013/ doi: 10.5194/angeo-31-1061-2013

Jacobi, C. (2012). 6 year mean prevailing winds and tides measured by VHF meteor radar over Collm (51.3N, 13.0E). *J. Atmos. Solar-Terrestrial Phys.*, *78-79*, 8–18. Retrieved from http://www.sciencedirect.com/science/article/pii/S1364682611001210 doi: https://doi.org/10.1016/j.jastp.2011.04.010

Lieberman, R. S., Riggin, D. M., Nguyen, V., Palo, S. E., Siskind, D. E., Mitchell, N. J., ... Livesey, N. J. (2017, apr). Global observations of 2 day wave coupling to the diurnal tide in a high-altitude forecast-assimilation system. *J. Geophys. Res. Atmos.*, *122*(8), 4135–4149. Retrieved from http://doi.wiley.com/10.1002/2016JD025144 doi: 10.1002/2016JD025144

Lilienthal, F., & Jacobi, C. (2015). Meteor radar quasi 2-day wave observations over 10 years at Collm (51.3° N, 13.0° E). *Atmos. Chem. Phys.*, *15*(17), 9917–9927. doi: 10.5194/acp-15-9917-2015

Manson, A. H., Meek, C. E., Gregory, J. B., & Chakrabarty, D. K. (1982). Fluctuations in tidal (24-, 12-h) characteristics and oscillations (8-h-5-d) in the mesosphere and lower thermosphere (70–110 km): Saskatoon (52°N, 107°W), 1979–1981. *Planet. Space Sci.*, *30*(12), 1283–1294. Retrieved from http://www.sciencedirect.com/science/article/pii/0032063382901027 doi: https://doi.org/10.1016/0032-0633(82)90102-7

Moudden, Y., & Forbes, J. M. (2014). Quasi-two-day wave structure, interannual variability, and tidal interactions during the 2002–2011 decade. *J. Geophys. Res.*, *119*(5), 2241–2260. doi: 10.1002/2013JD020563

Muller, H. G. (1972). A discussion on D and E region winds over Europe -

Long-period meteor wind oscillations. *Philos. Trans. R. Soc. London. Ser. A, Math. Phys. Sci.*, *271*(1217), 585–599. Retrieved from https://royalsocietypublishing.org/doi/abs/10.1098/rsta.1972.0026 doi: 10.1098/rsta.1972.0026

Nguyen, V. A., Palo, S. E., Lieberman, R. S., Forbes, J. M., Ortland, D. A., & Siskind, D. E. (2016, jul). Generation of secondary waves arising from nonlinear interaction between the quasi 2 day wave and the migrating diurnal tide. *J. Geophys. Res. Atmos.*, *121*(13), 7762–7780. Retrieved from http://doi.wiley.com/10.1002/2016JD024794 doi: 10.1002/2016JD024794

Palo, S. E., Roble, R. G., & Hagan, M. E. (1999). Middle atmosphere effects of the quasi-two-day wave determined from a General Circulation Model. *Earth, Planets Sp.*, *51*(7-8), 629–647. Retrieved from https://doi.org/10.1186/BF03353221 doi: 10.1186/BF03353221

Pancheva, D., Mukhtarov, P., & Siskind, D. E. (2018). Climatology of the quasi-2-day waves observed in the MLS/Aura measurements (2005–2014). *J. Atmos. Solar-Terrestrial Phys.*, *171*(April 2017), 210–224. Retrieved from https://doi.org/10.1016/j.jastp.2017.05.002 doi: 10.1016/j.jastp.2017.05.002

Pancheva, D., Mukhtarov, P., Siskind, D. E., & Smith, A. K. (2016). Global distribution and variability of quasi 2 day waves based on the NOGAPS-ALPHA reanalysis model. *J. Geophys. Res. Sp. Phys.*, *121*(11), 11,422–11,449. doi: 10.1002/2016JA023381

Pedatella, N. M., & Forbes, J. M. (2012). The quasi 2 day wave and spatial-temporal variability of the OH emission and ionosphere. *J. Geophys. Res. Sp. Phys.*, *117*(1), 1–11. doi: 10.1029/2011JA017186

Pfister, L. (1985). Baroclinic Instability of Easterly Jets with Applications to the Summer Mesosphere. *J. Atmos. Sci.*, *42*(4), 313–330. Retrieved from https://doi.org/10.1175/1520-0469(1985)042{\%}3C0313:BIOEJW{\%}3E2.0.CO;2 doi: 10.1175/1520-0469(1985)042⟨0313:BIOEJW⟩2.0.CO;2

Plumb, R. A. (1983). Baroclinic Instability of the Summer Mesosphere: A Mechanism for the Quasi-Two-Day Wave? *J. Atmos. Sci.*, *40*(1), 262–270. Retrieved from https://doi.org/10.1175/1520-0469(1983)040{\%}3C0262:BIOTSM{\%}3E2.0.CO;2 doi: 10.1175/1520-0469(1983)040⟨0262:BIOTSM⟩2.0.CO;2

Randel, W. J. (1994). Observations of the 2-Day Wave in NMC Stratospheric Analyses. *J. Atmos. Sci.*, *51*(2), 306–313. Retrieved from https://doi.org/10.1175/1520-0469(1994)051{\%}3C0306:OOTDWI{\%}3E2.0.CO;2 doi: 10.1175/1520-0469(1994)051⟨0306:OOTDWI⟩2.0.CO;2

Salby, M. L. (1981). Rossby Normal Modes in Nonuniform Background Configurations. Part II. Equinox and Solstice Conditions. *J. Atmos. Sci.*, *38*(9), 1827–1840. Retrieved from http://journals.ametsoc.org/doi/abs/10.1175/1520-0469(1981)038{\%}3C1827:RNMINB{\%}3E2.0.CO;2 doi: 10.1175/1520-0469(1981)038⟨1827:RNMINB⟩2.0.CO;2

Salby, M. L., & Callaghan, P. F. (2001). Seasonal Amplification of the 2-Day Wave: Relationship between Normal Mode and Instability. *J. Atmos. Sci.*, *58*(14), 1858–1869. Retrieved from https://doi.org/10.1175/1520-0469(2001)058{\%}3C1858:SAOTDW{\%}3E2.0.CO;2 doi: 10.1175/1520-0469(2001)058⟨1858:SAOTDW⟩2.0.CO;2

Salby, M. L., & Roper, R. G. (1980). Long-Period Oscillations in the Meteor Region. *J. Atmos. Sci.*, *37*(1), 237–244. Retrieved from https://doi.org/10.1175/1520-0469(1980)037{\%}3C0237:LPOITM{\%}3E2.0.CO;2 doi: 10.1175/1520-0469(1980)037⟨0237:LPOITM⟩2.0.CO;2

Teitelbaum, H., & Vial, F. (1991, aug). On tidal variability induced by nonlinear interaction with planetary waves. *J. Geophys. Res.*, *96*(A8), 169–178. Retrieved from http://doi.wiley.com/10.1029/91JA01019 doi: 10.1029/91JA01019

Teitelbaum, H., Vial, F., Manson, A. H., Giraldez, R., & Massebeuf, M. (1989). Non-linear interaction between the diurnal and semidiurnal tides: terdiurnal and diurnal secondary waves. *J. Atmos. Terr. Phys.*, *51*(7), 627–634. Retrieved from http://www.sciencedirect.com/science/article/pii/0021916989900615 doi: https://doi.org/10.1016/0021-9169(89)90061-5

Torrence, C., & Compo, G. P. (1998). A Practical Guide to Wavelet Analysis. *Bull. Am. Meteorol. Soc.*, *79*(1), 61–78. doi: 10.1175/1520-0477(1998)079⟨0061:APGTWA⟩2.0.CO;2

Tunbridge, V. M., Sandford, D. J., & Mitchell, N. J. (2011). Zonal wave numbers of the summertime 2 day planetary wave observed in the mesosphere by EOS Aura Microwave Limb Sounder. *J. Geophys. Res. Atmos.*, *116*(11), 1–16. doi: 10.1029/2010JD014567

Yu, Y., Wan, W., Ning, B., Liu, L., Wang, Z., Hu, L., & Ren, Z. (2013). Tidal wind mapping from observations of a meteor radar chain in December 2011. *J. Geophys. Res. Sp. Phys.*, *118*(5), 2321–2332. Retrieved from https://agupubs.onlinelibrary.wiley.com/doi/abs/10.1029/2012JA017976 doi: 10.1029/2012JA017976

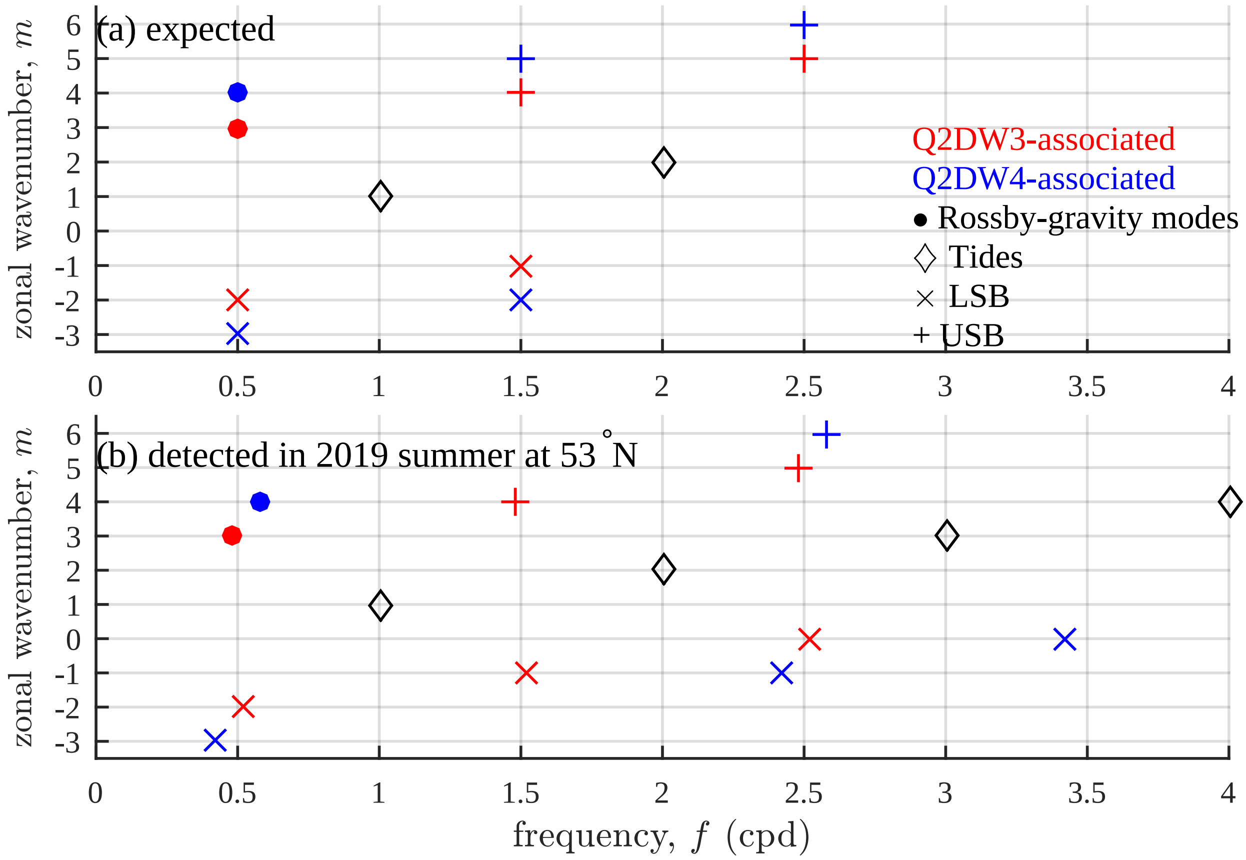

Figure 1: (a) Distribution of expected Q2DWs and associated secondary waves from non-linear interactions with tides in f-m plane, (b) waves detected in 2019 summer at 53°N consistently through two approaches (cf, Section 3).

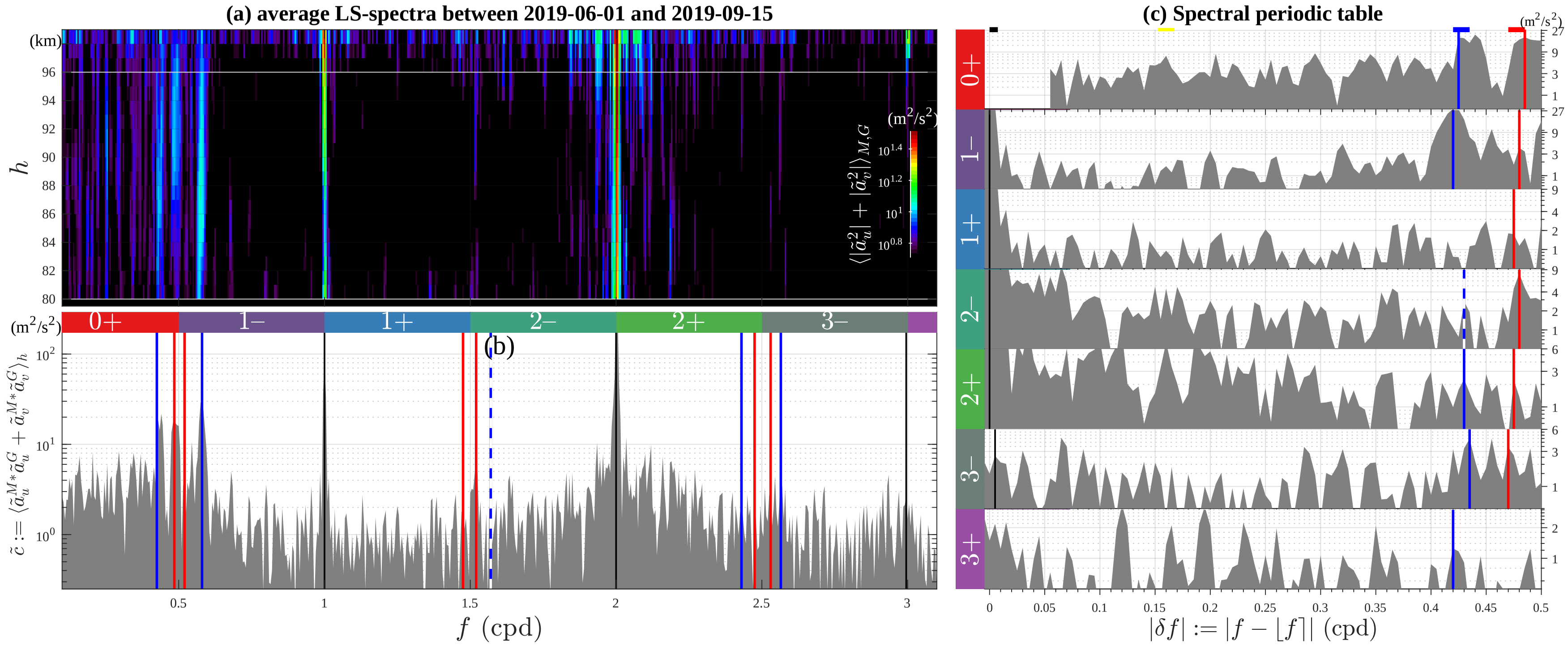

Figure 2: (a) Lomb-Scargle spectra $\langle|\tilde{a}_u^2|+|\tilde{a}_v^2|\rangle_{M,G}$, averaged between the two longitudes, Mohe and Germany, (b) altitude average of the cross-spectrum $\tilde{c}{:=}\langle\tilde{a}_u^{M*}\tilde{a}_u^G{+}\tilde{a}_v^{M*}\tilde{a}_v^G\rangle_h$, and (c) a periodic table representation of (b). (b) is divided into pieces denoted by the color bars on the top of the panel and labeled as '0+', '1−',... Each of the pieces is zoomed in and displayed in (c) as one row labeled on the very left. In (c) the x-axis represents $|\delta f|{:=}|f{-}\lfloor f \rceil|$, namely, the distance between f and its nearest integer $\lfloor f \rceil$. In (b,c), the vertical blue, red and black lines indicate three families of spectral peaks. Peaks from the same family share the same $|\delta f|$ value, and are used to diagnose the m through two approaches and specified in Table 1. Diagnoses from the two approaches are consistent at some peaks but inconsistent at the others, denoted by the solid and dashed lines, respectively. The white horizontal white lines in (a) indicate the spectrum used for calculating (b). See Section 3 for details.

Table 1: Wavenumber estimation through two approaches: m^{PDT} vs. m^f

$N\pm$	f (cpd)	T (hr)	$\sqrt{\lvert\tilde{c}\rvert}$ (m/s)	m^{PDT}	m^f	δm (Eq. 9)	$m^{PDT} \approx m^f$ (δm <0.5)	potential wave*
1±	1.000	24.0	9.3	0.95+3.31Z	1	0.05	✓	24hr migrating tide (DW1)
2±	2.000	12.0	20.6	1.89+3.31Z	2	0.11	✓	12hr migrating tide (SW2)
3±	2.995	8.0	1.6	0.15+3.31Z	3	0.46	✓	8hr migrating tide (TW3)
4±	4.000	6.0	1.1	0.25+3.31Z	4	0.44	✓	6hr migrating tide (QW4)
0+	0.425	56.5	4.3	0.54+3.31Z	−3	0.23	✓	DW1–Q2DW4
1−	0.580	41.4	5.5	1.14+3.31Z	4	0.45	✓	Q2DW4
2−	1.570	15.3	1.7	2.65+3.31Z	5	0.96	×	DW1+Q2DW4
2+	2.430	9.9	1.5	2.57+3.31Z	−1	0.26	✓	TW3–Q2DW4
3−	2.565	9.4	2.1	2.74+3.31Z	6	0.05	✓	SW2+Q2DW4
3+	3.420	7.0	1.1	0.25+3.31Z	0	0.25	✓	QW4–Q2DW4
0+	0.485	49.5	4.4	2.72+3.31Z	3	0.28	✓	Q2DW3
1−	0.520	46.2	2.0	0.93+3.31Z	−2	0.38	✓	DW1–Q2DW3**
1+	1.475	16.3	1.3	1.00+3.31Z	4	0.31	✓	DW1+Q2DW3***
2−	1.520	15.8	2.8	2.55+3.31Z	−1	0.25	✓	SW2–Q2DW3
2+	2.475	9.7	1.5	1.57+3.31Z	5	0.12	✓	SW2+Q2DW3
3−	2.530	9.5	1.9	0.34+3.31Z	0	0.34	✓	TW3–Q2DW3

*In the last column, the symbols '–' and '+' represent the LSB- and USB-generating interactions between the waves at the flanks of the symbols, respectively.

** also known as Q2DE2

*** also explained as SW2–Q2DE2 interaction

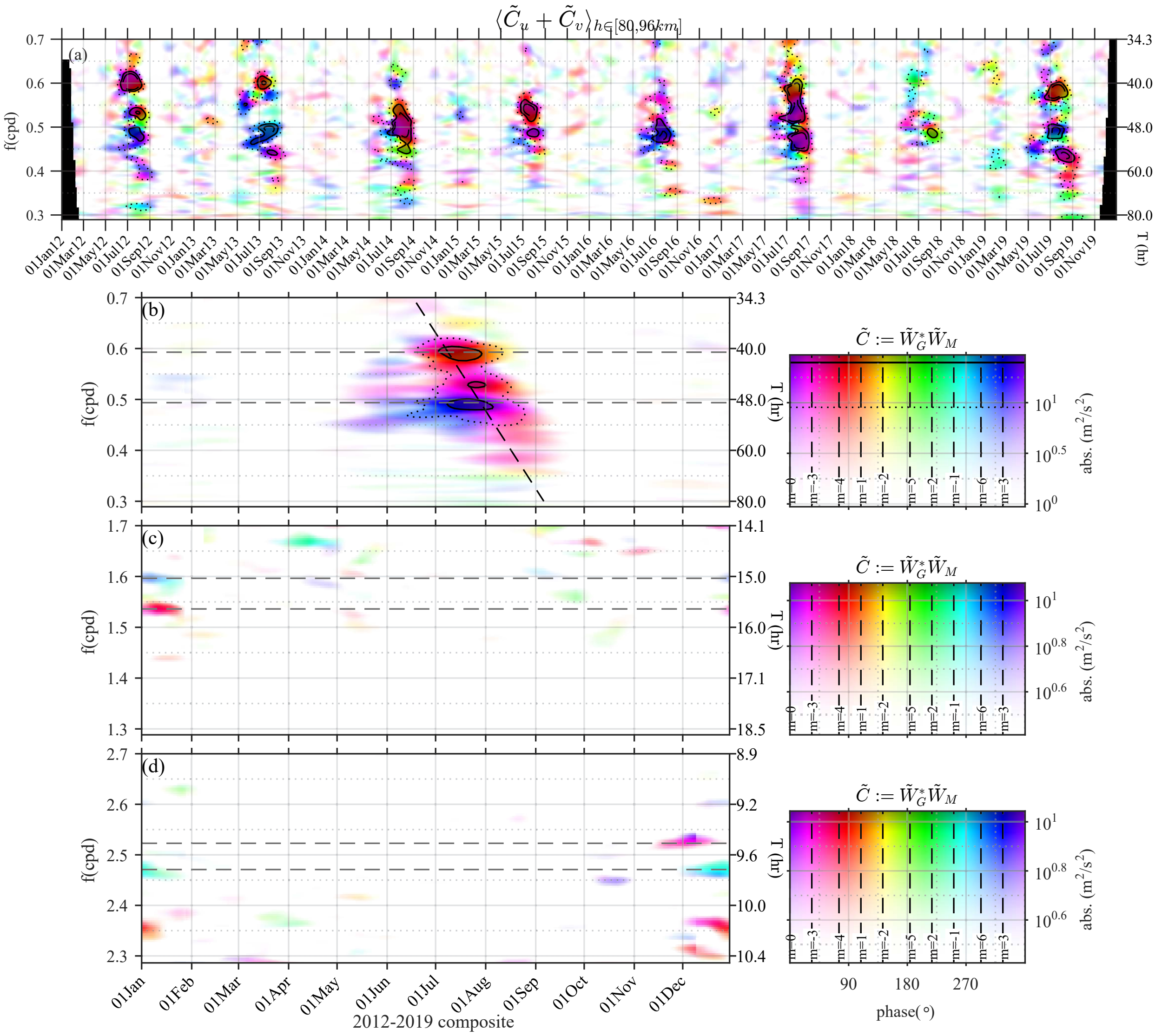

Figure 3: (a) 2012–2019 composited $\langle\tilde{C}_u+\tilde{C}_v\rangle_h$, namely, the sum of the cross-wavelet spectra of u and v wind components between the two longitudes, averaged in the altitude range $h\in$[80,96km] and frequency range $f\in \Delta f$:=[0.3 0.7cpd]. (b) the composited spectrum of (a). (c,d) same plots as (b) but in the frequency ranges Δf+1 and Δf+2, respectively. (a) and (b) share the same color-code map, in which the dotted, solid and dashed black isolines denote amplitudes at $\sqrt{|\tilde{C}|}$=3, 4, and 5m/s.

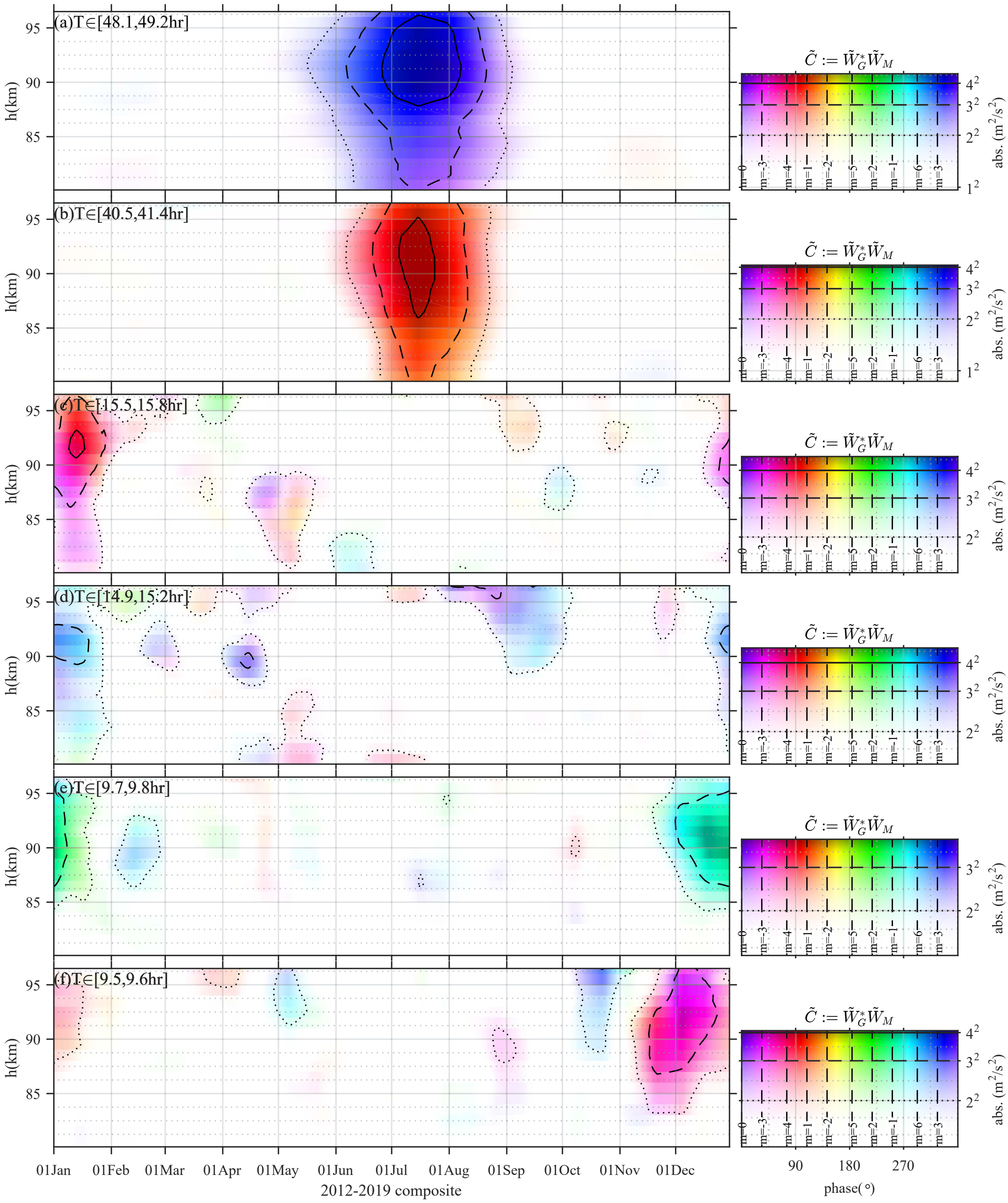

Figure 4: Multi-year composited $\tilde{C}_u + \tilde{C}_v$, as a function of month and altitude at six periods indicated by the horizontal dashed lines in Figures 3b–d.